

Competing pairing interactions responsible for the large upper critical field in a stoichiometric iron-based superconductor, $\text{CaKFe}_4\text{As}_4$

Matthew Bristow,^{1,*} William Knafo,² Pascal Reiss,¹ William Meier,^{3,4}
Paul C. Canfield,^{3,4} Stephen J. Blundell,¹ and Amalia I. Coldea^{1,†}

¹*Clarendon Laboratory, Department of Physics, University of Oxford, Parks Road, Oxford OX1 3PU, UK*

²*Laboratoire National des Champs Magnétiques Intenses (LNCMI), CNRS-UJF-UPS-INSA, Toulouse, France*

³*Ames Laboratory, Iowa State University, Ames, Iowa 50011, USA*

⁴*Department of Physics and Astronomy, Iowa State University, Ames, Iowa 50011, USA*

(Dated: March 9, 2020)

The upper critical field of multi-band superconductors is an important quantity that can reveal the details about the nature of the superconducting pairing. Here we experimentally map out the complete upper critical field phase diagram of a stoichiometric superconductor, $\text{CaKFe}_4\text{As}_4$, up to 90 T for different orientations of the magnetic field and at temperatures down to 4.2 K. The upper critical fields are extremely large, reaching values close to $\sim 3T_c$ at the lowest temperature, and the anisotropy decreases dramatically with temperature leading to essentially isotropic superconductivity at 4.2 K. We find that the temperature dependence of the upper critical field can be well described by a two-band model in the clean limit with band coupling parameters favouring intraband over interband interactions. The large Pauli paramagnetic effects together with the presence of the shallow bands is consistent with the stabilization of an FFLO state at low temperatures in this clean superconductor.

The upper critical field, H_{c2} , is an important property of superconductors that defines their limit for practical applications. It also describes the complex interplay between different pairing gaps and symmetry and can shed light on the nature of the superconducting mechanism. Furthermore, the temperature dependence of the upper critical field can also provide evidence for the presence of the Fulde-Ferrell-Larkin-Ovchinnikov (FFLO) state [1, 2] in which the order parameter varies in space. The iron-based superconductors have unusually large values of the upper critical field which reveal exotic effects caused by the interplay of orbital and paramagnetic pair-breaking in multiband superconductors with unconventional pairing symmetry [3]. They also provide the right conditions for the FFLO state to develop in clean materials due to the likely presence of shallow bands [4] and very large Pauli paramagnetic effects [1].

$\text{CaKFe}_4\text{As}_4$ is a clean and stoichiometric superconductor with a relatively high $T_c = 35$ K and it belongs to a new family of 1144 iron-based superconductors [5]. This system lacks long-ranged magnetic order or a nematic electronic state at low temperatures [5–11] but upon doping with Ni a hedgehog magnetic structure is stabilized [9, 12, 13]. $\text{CaKFe}_4\text{As}_4$ has an exceptionally large critical current density due to the strong point-like defects caused by local structural site effects as well as surface pinning [14–16]. Due to reduced symmetry compared with the 122 family of iron-based superconductors, $\text{CaKFe}_4\text{As}_4$ is predicted to have up to ten different bands (Fig. 1(e) and Fig. 4 in the Appendix). However, angle resolved photoemission spectroscopy detects a Fermi surface composed of three hole pockets and two electron pockets. The superconducting gaps are nearly isotropic and different for each of the Fermi surface sheets [4]. The presence of electron and hole sheets supports a spin resonance corresponding to the (π, π) nesting wave vector detected by neutron diffraction [6] and promotes a s_{\pm} superconducting pairing symmetry

in $\text{CaKFe}_4\text{As}_4$. Thus, this clean system is a model system for understanding the effect of pairing on its upper critical field.

In order to understand the superconducting properties of $\text{CaKFe}_4\text{As}_4$ we have measured the upper critical fields for two orientations in magnetic fields up to 90 T using electrical transport measurements. These experimental studies provide a complete $H_{c2}(T)$ phase diagram and allow us to model the entire temperature dependence, as previous work in magnetic fields up to 60 T could not reach the low temperature region [7]. We find that $\text{CaKFe}_4\text{As}_4$ is highly isotropic at the lowest temperature. A two-band model describes the dependence of the upper critical fields for both directions and the band coupling parameters indicate the presence of different pairing channels. At low temperatures, the upper critical field does not saturate but shows an upturn, consistent with the emergence of a FFLO state in $\text{CaKFe}_4\text{As}_4$.

Experimental details. Single crystals of $\text{CaKFe}_4\text{As}_4$ were grown in the Ames Laboratory, as discussed elsewhere [5, 17]. Robust electrical contacts were achieved using indium solder, giving contact resistances of less than 0.5Ω . Samples were measured using the standard 4- and 5-point ac lock-in techniques and a current of 1 mA. We have investigated several high quality single crystals, with large residual resistivity ratios ~ 14.5 ($RRR = \rho(300\text{K})/\rho(36\text{K})$), small residual resistivity, $\rho_0 \sim 9.4 \mu\Omega\text{cm}$, and sharp superconducting transitions, $\Delta T_c \sim 0.1$ K (see Figs. 1(f) and 5(c) in the Appendix). Transport measurements were performed in Oxford up to 16 T in a Quantum Design PPMS in constant magnetic fields and for different magnetic field orientations ($H||c$ and $H||(ab)$). Pulsed magnetic field measurements were performed at LNCMI Toulouse, using a 70 T single coil and a 90 T dual coil at constant temperatures below 35 K for both field orientations. Magnetic fields up to 90 T were produced by using current pulses through two different solenoid coils (an example is shown in Fig. 6 in the Appendix).

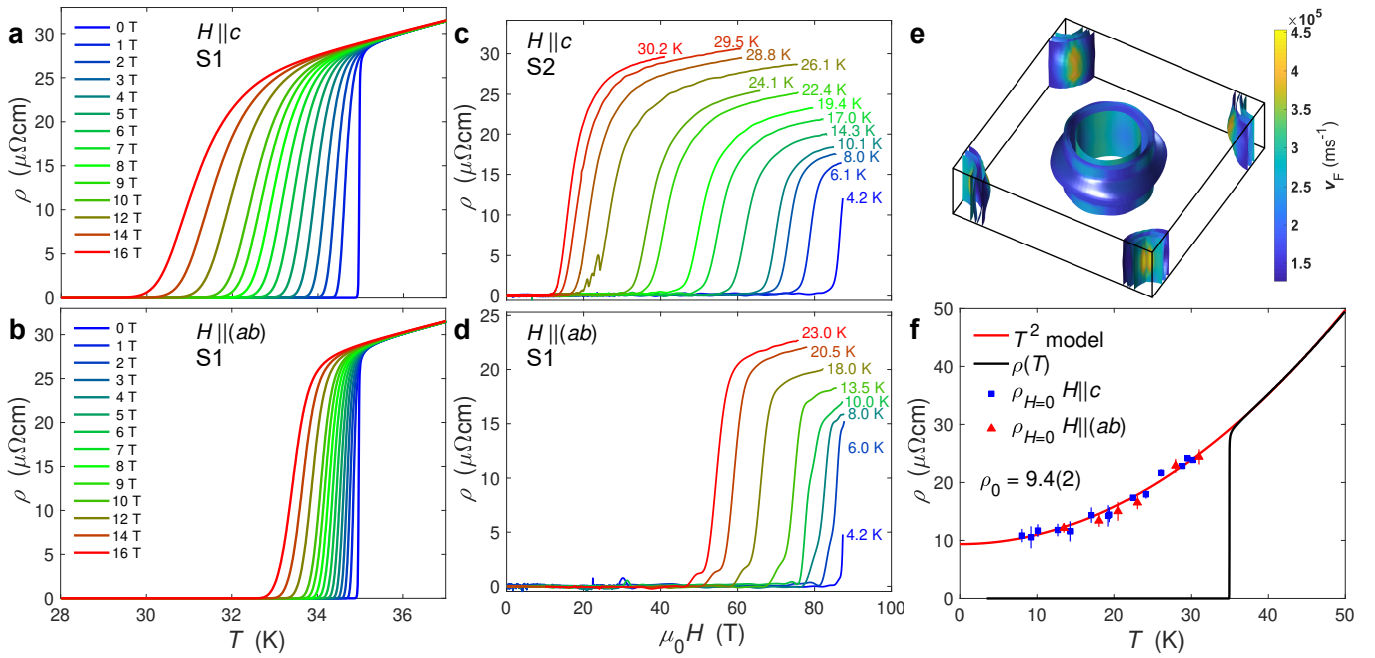


FIG. 1. Resistivity versus temperature for $\text{CaKFe}_4\text{As}_4$ (S1) at different constant magnetic fields for (a) $H||c$ and (b) $H||(ab)$. Resistivity versus magnetic field at constant temperatures measured concomitantly in pulsed fields up to 90 T, for (c) $H||c$ (S2) and (d) $H||(ab)$ (S1). (e) Fermi surface of $\text{CaKFe}_4\text{As}_4$ using experimental lattice parameters (as detailed in Fig. 4 in the Appendix). The colours reflect the variation of the Fermi velocity. (f) Resistivity against temperature for sample S1 together with the zero-field extrapolated values from high fields shown in (c) and (d) (see also Fig. 5(d) in the Appendix). The zero-temperature resistivity ρ_0 is estimated as $9.4(2) \mu\Omega\text{cm}$ using a Fermi-liquid T^2 behaviour (red line in (f)).

Upper critical field from transport measurements.

Fig. 1 shows resistivity against temperature for different fixed magnetic fields for orientations of the sample in relation to the applied magnetic field. As the magnetic field increases the superconducting transition becomes broader and suppressed faster for $H||c$ by 5 K in 16 T (Fig. 1(a)), as compared with the $H||(ab)$ case for which H_{c2} only changes by 2 K in 16 T (Fig. 1(b)), as the orbital effects are less effective in suppressing superconductivity in this orientation. These data are used to extract the upper critical field near T_c , defined as the offset field, as shown in Fig. 5(a) and (b) in the Appendix. Due to the high crystallinity of our samples that display sharp superconducting transitions, we find that the critical temperature from magnetization measurements is similar to the offset temperature determined from transport measurements (Fig. 5(a)). In order to completely suppress the superconductivity of $\text{CaKFe}_4\text{As}_4$ we have used pulsed magnetic fields up to 90 T. Resistivity data against magnetic fields up to 90 T measured at fixed temperature are shown in Fig. 1(c) and 1(d) for the two different orientations. Despite the strong disparity in the degree of suppression of superconductivity between the two field directions close to T_c , at the lowest measurable temperature of 4.2 K the normal state is reached at a similar field ~ 85 T for both orientations.

Upper critical field phase diagram. Based on these experimental data, we have constructed the complete upper critical field phase diagram of $\text{CaKFe}_4\text{As}_4$ down to 4.2 K as shown

in Fig. 2(a) for the two orientations. Our results are in good agreement with previous studies up to 60 T for both offset and onset critical fields [7] (see Fig. 9(a) and (b)) and reveal extremely large upper critical fields, reaching almost $\sim 3T_c$ at the lowest temperatures. These values are above the Pauli paramagnetic limit, $\sim 1.85T_c$, estimated to be ~ 65 T for a single-band superconductor and assuming $g=2$ and the weak coupling limit. The anisotropy of the upper critical field, defined as the ratio of the upper critical field for different orientations, $\Gamma = H_{c2}^{ab}/H_{c2}^c$, drops dramatically with decreasing temperature from ~ 4 to 1, as shown in Fig. 2(b). Interestingly, the upper critical fields for the two orientations cross at $T \sim 4.2$ K, leading to isotropic superconducting behaviour in the low temperature limit. This phenomenon has been found in optimally doped iron-based superconductors, such as $\text{FeSe}_{0.5}\text{Te}_{0.5}$ [18, 19] and $(\text{Ba,K})\text{Fe}_2\text{As}_2$ [20]. This behaviour reflects the large Pauli paramagnetic effects in iron-based superconductors and the influence of Fermi surface details on limiting the orbital effects [20]. The Fermi surface of $\text{CaKFe}_4\text{As}_4$ has significant warping for the outer electron and hole band that can potentially allow circulating currents out of plane (see Fig. 4(d) in the Appendix). Furthermore, the calculated anisotropy of the penetration depth based on plasma frequencies (as in Ref. 21) is $\Gamma = \lambda_c/\lambda_{ab} \sim 4.5$, (see Fig. 4 in the Appendix) similar to the measured anisotropy close to T_c (Fig. 2(b)), suggesting that the Fermi surface details play an important role in understanding its superconducting proper-

ties.

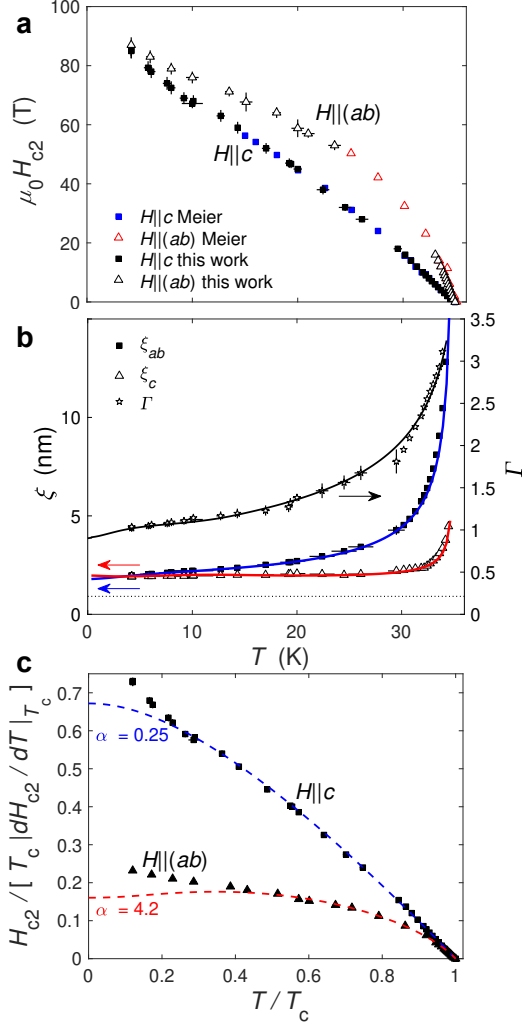


FIG. 2. (a) Upper critical fields as a function of temperature in CaKFe₄As₄ when $H||c$ (solid squares) and $H||(ab)$ (open triangles), together with previously reported data measured up to 60 T from Ref. 7. (b) The temperature dependence of coherence length extracted close to T_c , as described in the SM. The $H_{c2}(T = 0)$ value were used to find the zero-temperature coherence lengths. The horizontal dashed line represents the 3D-2D crossover when coherence length $\sim c/\sqrt{2}$. The anisotropy $\Gamma = H_{c2}^b/H_{c2}^c$ on the right axis approaches $\Gamma = 1$ at ~ 4.2 K. Solid lines are guide to the eye. (c) Upper critical fields for $H||c$ (black squares) and $H||(ab)$ (black triangles) scaled by the superconducting transition temperature, T_c , and the slope near T_c from the WHH model against reduced temperature T/T_c . The dashed blue and red lines are fits to the WHH model for $H||c$ and $H||(ab)$ using different values of α . Deviation from the WHH model occurs at low temperatures for both field orientations.

Having experimentally determined the upper critical fields for different orientations in magnetic field, we can extract the associated coherence lengths in different temperature regimes, as detailed in the Appendix. In the vicinity of T_c , the Ginzburg-Landau coherence lengths shown in Fig. 2(b) are $\xi_{ab}^{GL} = 1.66(4)$ nm and $\xi_c^{GL} = 0.53(2)$ nm for CaKFe₄As₄,

similar to previously reported values [7]. In the low temperature limit, we find coherence lengths of $\xi_{ab} = 1.83(3)$ nm and $\xi_c = 1.87(6)$ nm, as shown in Fig. 7 in the Appendix. This demonstrates the presence of an isotropic superconducting state at lowest temperature in CaKFe₄As₄. The coherence lengths approach the 3D to 2D crossover close to $c/\sqrt{2} \sim 0.911$ nm, as shown in Fig. 2(b) [5, 22]). The low temperature extracted ξ values are larger than ~ 0.7 nm reported from STM measurements, which probe locally the vortex lattice rather than an overall averaged effect [23]. Knowing the coherence length, allows us to estimate the depairing current density, J_d , as described in the Appendix [24]. Previous magnetisation data reported a value of $\mu_0 H_{c1} = 22(1)$ mT when $H||c$ at low temperature which, combined with H_{c2} reported here, give $\kappa = 99(2)$ and $\lambda = 183(6)$ nm. Using this value for the penetration depth and $\xi = 1.86(3)$ nm gives $J_d = 1.61(9) \times 10^8$ A/cm², which is one of the largest among iron-based superconductors. This supports the extremely large critical current densities, reported previously for CaKFe₄As₄ in Ref. [14]. The small coherence length of CaKFe₄As₄ is compatible with the presence of the large upper critical field, consistent with small Fermi velocities and high T_c values of CaKFe₄As₄ ($\xi \sim \hbar v_F / (2\pi k_B T_c)$) [1]. Surface superconductivity can survive in a thin layer of thickness $\sim \xi$ in systems with clean surfaces and it can lead to a critical field larger than H_{c2} . In order to establish the importance of those effects, future angular-dependent studies would be necessary to identify the role played by surface superconductivity in CaKFe₄As₄ close to T_c . Using the extrapolated zero-temperature normal state resistivity $\rho_0 \sim 9.4 \mu\Omega\text{cm}$ in Fig. 1(f) and carrier concentrations from Ref. 7, we can estimate a mean free path of $\ell = 26.6$ nm. Since the mean free path due to elastic scattering from impurities is far larger than the coherence length, $\xi(0) \ll \ell$, CaKFe₄As₄ can be described as being in the clean limit. Resistivity data in Fig. 1(f) show also a sharp superconducting transition indicating a high quality single crystal. Furthermore, the extrapolated high-field resistivity at low temperatures (see Fig. 4(d) in the Appendix) displays a T^2 dependence indicative of a Fermi-liquid behaviour that extends up to ~ 55 K.

In order to assess the role of orbital and Pauli paramagnetic effects on the upper critical field of CaKFe₄As₄ we first describe the temperature dependence of the upper critical field using the three-dimensional Werthamer-Helfand-Hohenberg (WHH) model [25], with the inclusion of spin paramagnetism effects. The slope close to T_c ($H_{c2}' = -|dH_{c2}/dT|_{T=T_c}$) is used to estimate the zero-temperature orbital upper critical field and $H_{c2}^{\text{orb}} = 0.73H_{c2}'$ for the clean limit ($0.69H_{c2}'$ in the dirty limit) for a single-band weak-coupling superconductor with ellipsoidal Fermi surface [26]. We find that the orbital pair breaking dominates the temperature dependence for $H||c$ down to 10 K, below which it deviates, as shown in Fig. 2(c). However, when the magnetic field is aligned along the conducting (ab) plane, a Pauli pair breaking contribution has to be included which reduces the orbital-limited critical field by $\mu_0 H_P = \mu_0 H_{c2}^{\text{orb}} / \sqrt{1 + \alpha^2}$, where α is the Maki pa-

parameter. The extracted Maki parameter α is small where the orbital effects dominate ($\alpha \sim 0.25$ for $H||c$), but it becomes significant reaching $\alpha = 4.2$ for $H||(ab)$ (see Fig. 2(c)). This value is close to that of $\text{FeSe}_{0.6}\text{Te}_{0.6}$ single crystals where $\alpha \sim 5.5$ suggesting that the upper critical field is dominated by Pauli paramagnetic effects [27]. Strong paramagnetic effects are an important signature of optimally doped iron-based superconductors [28–32]. For a clean isotropic single-band, the Maki parameter is given by $\alpha = \pi^2 \Delta / (4E_F)$. The values of the measured superconducting gap Δ varies between 2.4 – 13 meV whereas the Fermi energies vary significantly for different bands, being smallest for the inner hole band, α (~ 3 meV) and the shallow electron band δ (~ 10 meV) [4, 33]. The band structure calculation predicts four electron pockets centred at the M point, as shown in Fig. 4 in the Appendix. Experimentally, only one electron pocket can be resolved in experiments due to a significant intrinsic linewidth and the fact that the bottom of these bands is located very close to Fermi level [4]. Thus, the presence of the shallow bands, together with the small Fermi energies E_F and large superconducting gap Δ create conditions for large α and Pauli pair-breaking.

Upper critical field described by a two-band model.

In order to describe the complete temperature dependence of $H_{c2}(T)$ for $\text{CaKFe}_4\text{As}_4$, including the upturn below ~ 10 K for both orientations, a two-band model in the clean limit is considered, as detailed in Ref. 1 and in the Appendix. This model accounts for the presence of two different bands, with interband scattering ($\lambda_{11}, \lambda_{22}$) and intraband effects ($\lambda_{12}, \lambda_{21}$) and includes paramagnetic effects and allows for the presence of an FFLO inhomogeneous state at high-fields and low temperatures [1]. An FFLO state is characterized by a real-space modulation of the superconducting order parameter either in amplitude or phase such that the system energy is minimized under the constraints of a large Zeeman energy and superconducting condensation energy [2]. As the FFLO wave vector Q appears spontaneously below a certain temperature, T_{FFLO} , the spinodal instability line in $H_{c2}(T)$ at a finite Q acquires the characteristic upturn [1].

In most iron-based superconductors, the pairing is expected to be mediated by spin-fluctuations leading to a sign changing s_{\pm} order parameter. In this case, upper critical fields are generally described by dominant interband coupling parameters with $\lambda_{11} = \lambda_{22} = 0$ and $\lambda_{12} = \lambda_{21} \sim 0.5$ ($\lambda_{11}\lambda_{22} \ll \lambda_{12}\lambda_{21}$) [3, 7, 28, 29, 34, 35]. Furthermore, in these multiband systems orbital fluctuations can dominate the pairing interactions in certain conditions favouring a gap with equal sign on each pocket, resulting in the s^{++} pairing [36] ($\lambda_{11}\lambda_{22} \gg \lambda_{12}\lambda_{21}$).

To model the upper critical fields for both field orientations, we have considered different input parameters from previous experiments on $\text{CaKFe}_4\text{As}_4$. For example, the ratio between the extreme velocities of the Fermi surfaces is taken from ARPES experiments [33] and it gives a starting value of $\eta_c \sim 0.02$, which is the squared velocity ratio between the two bands. Upper critical field simulations have a strong sensitiv-

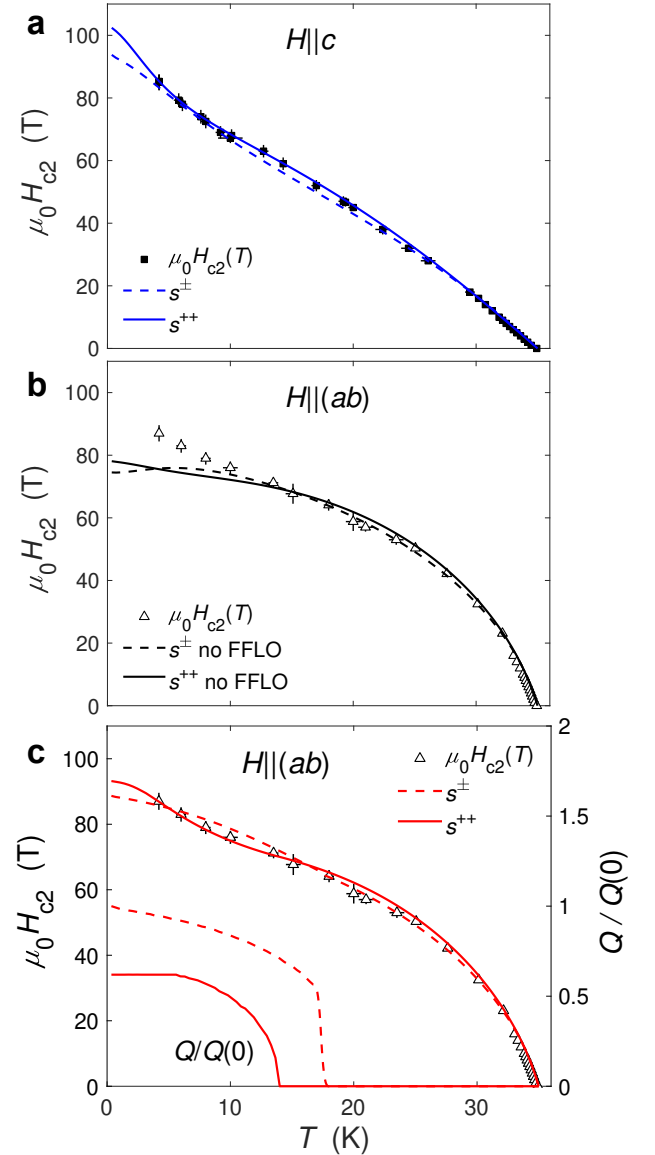


FIG. 3. Upper critical fields for (a) $H||c$ (solid squares) and (b) and (c) $H||(ab)$ (open triangles) described by the two-band model. The dotted lines correspond to s_{\pm} pairing ($\lambda_{11} = \lambda_{22} = 0$, $\lambda_{12} = \lambda_{21} \sim 0.5$, $\alpha_1 = 0.95$, $\alpha_2 = 0$ for $H||c$ and $\alpha_1 = 3.1$ and $\alpha_2 = 0.7$ for $H||(ab)$). Solid lines represent s^{++} pairing ($\lambda_{11} = 0.81$, $\lambda_{22} = 0.29$ and $\lambda_{12} = \lambda_{21} = 0.1$, $\alpha_1 = 0.5$ for $H||c$ and $\alpha_1 = 3.2$, $\alpha_2 = 0$ for $H||(ab)$). The values of η vary between ~ 0.02 in (a) and ~ 0.04 in (b). (c) The temperature dependence of the upper critical field including the emergence of the FFLO state for the two different pairing symmetries with the same parameters as in (b). The lower dashed and red line represents the scaled FFLO $Q/Q(0)$ modulation for $H||(ab)$ for the respective pairing (right axis).

ity to η values, as shown in Fig. 8 in the Appendix and it can change for different field orientations due to differences in the in-plane velocities on the Fermi surface (see Figs. 1(e) and 4 in the Appendix). We assume that $s=1$ (defined by Eq. 9 in the Appendix) for both field orientations and the starting values of the Maki parameters are those from the single band model of

$H_{c2}(T)$ in Fig. 2(c).

Firstly, the $H_{c2}(T)$ data are simulated for $\text{CaKFe}_4\text{As}_4$ using parameters corresponding to the s^\pm case (dashed lines Figs. 3(a) and 3(b)), which provide a reasonable representation of the observed behaviour for both orientations. However, we find that $H_{c2}(T)$ is best described using $\lambda_{11} = 0.81$, $\lambda_{22} = 0.29$ and $\lambda_{12} = \lambda_{21} = 0.1$ (solid lines in Figs. 3(a) and 3(b)), which is consistent with s^{++} pairing. For the later model, the constrained Fermi velocities are $v_1 \sim 380(20)$ meVÅ and $v_2 \sim 54(4)$ meVÅ when $H||c$, and $v_1 \sim 195(20)$ meVÅ and $v_2 \sim 41(4)$ meVÅ when $H||(ab)$ (see Table I). The values of v_2 are similar in both orientations, indicative of a strongly warped sheet (see Fig. 4 in the Appendix). On the other hand, v_1 is larger for $H||c$ and is close to ~ 360 meVÅ, reported for the α hole band from ARPES measurements [33]. The band coupling constants, $\lambda_{i,j}$ that describe our data suggest that the interband scattering due to spin-fluctuations is dominated by the intraband effects in $\text{CaKFe}_4\text{As}_4$, which can occur in the presence of strong orbital fluctuations [36]. For s^{++} pairing to overcome s^\pm pairing it normally requires the presence of strong disorder which leads to similar superconducting gaps on different Fermi surfaces [37]. Furthermore, the band coupling constants for the s^{++} case resemble those used to describe a two-band superconductor in the dirty limit [38]. However, $\text{CaKFe}_4\text{As}_4$ is clean, suggesting that disorder effects are negligible. Thus, based on the band coupling parameters, we conclude that orbital fluctuations may dominate over spin fluctuations.

When the magnetic field lies along the conducting planes, the low temperature upturn of $H_{c2}(T)$ in Fig. 3(b) cannot be fully captured by only considering the two-band model with large Pauli paramagnetic effects, $\alpha \sim 3.2$. The formation of the FFLO state in a system with a cylindrical Fermi surface requires a large Zeeman energy and a critical Maki's parameter of $\alpha_c = 4.76$ [2], compared to $\alpha_c = 1.8$ [39] for a three-dimensional Fermi surface. $\text{CaKFe}_4\text{As}_4$ has a complex Fermi surface with two-dimensional cylindrical and highly warped sheets and together with a large value of α creates the conditions for the emergence of an FFLO state [1]. A FFLO state can be realized in very clean materials with weak scattering of quasiparticles and it generally manifests as change in slope in the upper critical field at low temperatures [1]. We find indeed that in order to describe the upper critical field data of $\text{CaKFe}_4\text{As}_4$ over the entire temperature range, a FFLO state could be stabilized below $T_{\text{FFLO}} \sim 14$ K, as shown in Fig. 3(c). Possible contenders to support such an effect are the shallow electron Fermi surface pocket, δ , in the zone corner which is very close to the Fermi level (~ 10 meV) as well as the inner hole band α (~ 3 meV), as detected by ARPES measurements [4].

The temperature dependence of the upper critical field data in $\text{CaKFe}_4\text{As}_4$ implies that the intraband scattering is likely to dominate the interband scattering, the latter of which being promoted by spin fluctuations. In the presence of spin-orbit coupling the orbital fluctuations can lead to s^{++} pairing, as suggested for LiFeAs [40]. Usually s^{++} pairing results

in far lower critical fields than s^\pm pairing [1], so our results for $\text{CaKFe}_4\text{As}_4$ are somehow unusual as H_{c2} is almost $3T_c$ at the lowest temperature. The presence of several scattering channels in a multi-band system like $\text{CaKFe}_4\text{As}_4$ can increase the upper critical field to a much greater extent than in single gap superconductors, caused by the relative weight of different scattering channels. $\text{CaKFe}_4\text{As}_4$ theoretically has up to six large cylindrical hole bands, (with the equivalent of 50% hole doping in a 122 iron-based superconductor) providing a large density of states (see Fig. 1(e), Fig. 4 in the Appendix and Ref. 33) and it can also promote intraband scattering driven by orbital or electron-phonon couplings. On the other hand, the shallow bands in $\text{CaKFe}_4\text{As}_4$ are likely to be involved in the stabilization of the FFLO state. Thus, the temperature dependence of the upper critical field of $\text{CaKFe}_4\text{As}_4$ can reflect the behaviour of two dominant superconducting gaps that reside on different sheets of the cylindrical Fermi surface, possibly one on a large hole band and another one on a shallow small band.

In summary, we have experimentally mapped the upper critical fields of $\text{CaKFe}_4\text{As}_4$ up to 90 T and down to 4.2 K, providing a complete phase diagram for this stoichiometric superconductor. The anisotropy decreases dramatically with temperature, the system becoming essentially isotropic near 4 K. Upper critical fields are extremely large in this system, reaching close to $\sim 3T_c$ at the lowest temperature, well above the expectation based on conventional single-band superconductivity. Instead, the temperature dependence of the upper critical field can be described using by a two-band model in the clean limit. The band coupling constants suggest a dominant orbital pairing over spin fluctuations pairing in $\text{CaKFe}_4\text{As}_4$. Furthermore, for magnetic fields aligned in the conducting plane and due to large Pauli paramagnetic effects, we find that the temperature dependence of the upper critical field is consistent with the emergence of an FFLO state at low temperatures.

Acknowledgements We thank Alex Gurevich for helpful discussions related to the two-band modelling of the upper critical field and Jérôme Béard, Marc Nardone, Abdelaziz Zitouni for the technical support during the pulsed field experiments. This work was mainly supported by Oxford Centre for Applied Superconductivity. P.R. acknowledges the support of the Oxford Quantum Materials Platform Grant (EP/M020517/1). Part of this work was supported HFML-RU/FOM and LNCMI-CNRS, members of the European Magnetic Field Laboratory (EMFL) and by EPSRC (UK) via its membership to the EMFL (grant no. EP/N01085X/1). Part of this work at the LNCMI was supported by Programme Investissements d'Avenir under the program ANR-11-IDEX-0002-02, reference ANR-10-LABX-0037-NEXT. Work at Ames Laboratory was supported by the U.S. Department of Energy, Office of Basic Energy Science, Division of Materials Sciences and Engineering. Ames Laboratory is operated for the U.S. Department of Energy by Iowa State University under Contract No. DE-AC02-07CH11358. W.M. was supported by the Gordon and Betty Moore Foundations EPiQS

Initiative through Grant GBMF4411. We also acknowledge financial support of the John Fell Fund of the Oxford University. AIC acknowledges an EPSRC Career Acceleration Fellowship (EP/I004475/1) and Oxford Centre for Applied Superconductivity.

* corresponding author: matthew.bristow@physics.ox.ac.uk

† corresponding author: amalia.coldea@physics.ox.ac.uk

- [1] A. Gurevich, “Upper critical field and the Fulde-Ferrell-Larkin-Ovchinnikov transition in multiband superconductors,” *Phys. Rev. B* **82**, 184504 (2010).
- [2] Kok Wee Song and Alexei E. Koshelev, “Quantum FFLO State in Clean Layered Superconductors,” *Phys. Rev. X* **9**, 021025 (2019).
- [3] P. J. Hirschfeld, M. M. Korshunov, and I. I. Mazin, “Gap symmetry and structure of Fe-based superconductors,” *Reports on Progress in Physics* **74**, 124508 (2011).
- [4] Daixiang Mou, Tai Kong, William R. Meier, Felix Lochner, Lin-Lin Wang, Qisheng Lin, Yun Wu, S. L. Bud’ko, Ilya Eremin, D. D. Johnson, P. C. Canfield, and Adam Kaminski, “Enhancement of the Superconducting Gap by Nesting in $\text{CaKFe}_4\text{As}_4$: A New High Temperature Superconductor,” *Phys. Rev. Lett.* **117**, 277001 (2016).
- [5] A. Iyo, K. Kawashima, T. Kinjo, T. Nishio, S. Ishida, H. Fujihisa, Y. Gotoh, K. Kihou, H. Eisaki, and Y. Yoshida, “New-Structure-Type Fe-Based Superconductors: $\text{CaAFe}_4\text{As}_4$ ($A = \text{K, Rb, Cs}$) and $\text{SrAFe}_4\text{As}_4$ ($A = \text{Rb, Cs}$),” *J. Am. Chem. Soc.* **138**, 3410 (2016).
- [6] Kazuki Iida, Motoyuki Ishikado, Yuki Nagai, Hiroyuki Yoshida, Andrew D. Christianson, Naoki Murai, Kenji Kawashima, Yoshiyuki Yoshida, Hiroshi Eisaki, and Akira Iyo, “Spin Resonance in the New-Structure-Type Iron-Based Superconductor $\text{CaKFe}_4\text{As}_4$,” *Journal of the Physical Society of Japan* **86**, 093703 (2017).
- [7] W. R. Meier, T. Kong, U. S. Kaluarachchi, V. Taufour, N. H. Jo, G. Drachuck, A. E. Böhmer, S. M. Saunders, A. Sapkota, A. Kreyssig, M. A. Tanatar, R. Prozorov, A. I. Goldman, F. F. Balakirev, A. Gurevich, S. L. Bud’ko, and P. C. Canfield, “Anisotropic thermodynamic and transport properties of single crystalline $\text{CaKFe}_4\text{As}_4$,” *Phys. Rev. B* **94**, 064501 (2016).
- [8] Sergey L. Budko, Tai Kong, William R. Meier, Xiaoming Ma, and Paul C. Canfield, “ ^{57}Fe Mossbauer study of stoichiometric iron-based superconductor $\text{CaKFe}_4\text{As}_4$: a comparison to KFe_2As_2 and CaFe_2As_2 ,” *Philosophical Magazine* **97**, 2689–2703 (2017).
- [9] Sergey L. Bud’ko, Vladimir G. Kogan, Ruslan Prozorov, William R. Meier, Mingyu Xu, and Paul C. Canfield, “Coexistence of superconductivity and magnetism in $\text{CaK}(\text{Fe}_{1-x}\text{Ni}_x)_4\text{As}_4$ as probed by ^{57}Fe Mössbauer spectroscopy,” *Phys. Rev. B* **98**, 144520 (2018).
- [10] J. Cui, Q.-P. Ding, W. R. Meier, A. E. Böhmer, T. Kong, V. Borisov, Y. Lee, S. L. Bud’ko, R. Valentí, P. C. Canfield, and Y. Furukawa, “Magnetic fluctuations and superconducting properties of $\text{CaKFe}_4\text{As}_4$ studied by ^{75}As NMR,” *Phys. Rev. B* **96**, 104512 (2017).
- [11] W.-L. Zhang, W. R. Meier, T. Kong, P. C. Canfield, and G. Blumberg, “High- T_c superconductivity in $\text{CaKFe}_4\text{As}_4$ in absence of nematic fluctuations,” *Phys. Rev. B* **98**, 140501(R) (2018).
- [12] Q.-P. Ding, W. R. Meier, A. E. Böhmer, S. L. Bud’ko, P. C. Canfield, and Y. Furukawa, “NMR study of the new magnetic superconductor $\text{CaK}(\text{Fe}_{0.951}\text{Ni}_{0.049})_4\text{As}_4$: Microscopic coexistence of the hedgehog spin-vortex crystal and superconductivity,” *Phys. Rev. B* **96**, 220510(R) (2017).
- [13] Q.-P. Ding, W. R. Meier, J. Cui, M. Xu, A. E. Böhmer, S. L. Bud’ko, P. C. Canfield, and Y. Furukawa, “Hedgehog Spin-Vortex Crystal Antiferromagnetic Quantum Criticality in $\text{CaK}(\text{Fe}_{1-x}\text{Ni}_x)_4\text{As}_4$ Revealed by NMR,” *Phys. Rev. Lett.* **121**, 137204 (2018).
- [14] Shiv J. Singh, Matthew Bristow, William R. Meier, Patrick Taylor, Stephen J. Blundell, Paul C. Canfield, and Amalia I. Coldea, “Ultrahigh critical current densities, the vortex phase diagram, and the effect of granularity of the stoichiometric high- T_c superconductor $\text{CaKFe}_4\text{As}_4$,” *Phys. Rev. Materials* **2**, 074802 (2018).
- [15] N. Haberkorn, M. Xu, W. R. Meier, J. Schmidt, S. L. Bud’ko, and P. C. Canfield, “Effect of Ni doping on vortex pinning in $\text{CaK}(\text{Fe}_{1-x}\text{Ni}_x)_4\text{As}_4$ single crystals,” *Phys. Rev. B* **100**, 064524 (2019).
- [16] Shigeyuki Ishida, Akira Iyo, Hiraku Ogino, Hiroshi Eisaki, Nao Takeshita, Kenji Kawashima, Keiichi Yanagisawa, Yuuga Kobayashi, Koji Kimoto, Hideki Abe, Motoharu Imai, Jun-ichi Shimoyama, and Michael Eisterer, “Unique defect structure and advantageous vortex pinning properties in superconducting $\text{CaKFe}_4\text{As}_4$,” *npj Quantum Materials* **4**, 27 (2019).
- [17] W. R. Meier, T. Kong, S. L. Bud’ko, and P. C. Canfield, “Optimization of the crystal growth of the superconductor $\text{CaKFe}_4\text{As}_4$ from solution in the $\text{FeAs}-\text{CaFe}_2\text{As}_2-\text{KFe}_2\text{As}_2$ system,” *Phys. Rev. Materials* **1**, 013401 (2017).
- [18] A. Serafin, A. I. Coldea, A. Y. Ganin, M. J. Rosseinsky, K. Prasad, D. Vignolles, and A. Carrington, “Anisotropic fluctuations and quasiparticle excitations in $\text{FeSe}_{0.5}\text{Te}_{0.5}$,” *Phys. Rev. B* **82**, 104514 (2010).
- [19] Daniel Braithwaite, Grard Lapertot, William Knafo, and Ilya Sheikin, “Evidence for Anisotropic Vortex Dynamics and Pauli Limitation in the Upper Critical Field of $\text{FeSe}_{1-x}\text{Te}_x$,” *Journal of the Physical Society of Japan* **79**, 053703 (2010).
- [20] H. Q. Yuan, J. Singleton, F. F. Balakirev, S. A. Baily, G. F. Chen, J. L. Luo, and N. L. Wang, “Nearly isotropic superconductivity in $(\text{Ba,K})\text{Fe}_2\text{As}_2$,” *Nature* **457**, 565 (2009).
- [21] K. Hashimoto, A. Serafin, S. Tonegawa, R. Katsumata, R. Okazaki, T. Saito, H. Fukazawa, Y. Kohori, K. Kihou, C. H. Lee, A. Iyo, H. Eisaki, H. Ikeda, Y. Matsuda, A. Carrington, and T. Shibauchi, “Evidence for superconducting gap nodes in the zone-centered hole bands of kFe_2as_2 from magnetic penetration-depth measurements,” *Phys. Rev. B* **82**, 014526 (2010).
- [22] D. V. Suetin and I. R. Shein, “Electronic Properties and Fermi Surface for New Layered High-Temperature Superconductors $\text{CaAFe}_4\text{As}_4$ ($A = \text{K, Rb, and Cs}$): FLAPW-GGA Calculations,” *Journal of Superconductivity and Novel Magnetism* **4**, 1–10 (2017).
- [23] Antón Fente, William R. Meier, Tai Kong, Vladimir G. Kogan, Sergey L. Bud’ko, Paul C. Canfield, Isabel Guillamón, and Hermann Suderow, “Influence of multiband sign-changing superconductivity on vortex cores and vortex pinning in stoichiometric high- T_c $\text{CaKFe}_4\text{As}_4$,” *Phys. Rev. B* **97**, 134501 (2018).
- [24] Michael Tinkham, *Introduction to Superconductivity*, 2nd ed. (Dover Publications, 2004).
- [25] N. R. Werthamer, E. Helfand, and P. C. Hohenberg, “Temperature and purity dependence of the superconducting critical field, H_{c2} . iii. electron spin and spin-orbit effects,” *Phys. Rev.* **147**, 295–302 (1966).

- [26] E. Helfand and N. R. Werthamer, “Temperature and purity dependence of the superconducting critical field, H_{c2} . II,” *Physical Review* **147**, 288–294 (1966).
- [27] Seunghyun Khim, Jae Wook Kim, Eun Sang Choi, Yunkyu Bang, Minoru Nohara, Hidenori Takagi, and Kee Hoon Kim, “Evidence for dominant Pauli paramagnetic effect in the upper critical field of single-crystalline $\text{FeTe}_{0.6}\text{Se}_{0.4}$,” *Physical Review B* **81**, 1–5 (2010).
- [28] C. Tarantini, A. Gurevich, J. Jaroszynski, F. Balakirev, E. Bellingeri, I. Pallecchi, C. Ferdeghini, B. Shen, H. H. Wen, and D. C. Larbalestier, “Significant enhancement of upper critical fields by doping and strain in iron-based superconductors,” *Phys. Rev. B* **84**, 184522 (2011).
- [29] K. Cho, H. Kim, M. A. Tanatar, Y. J. Song, Y. S. Kwon, W. A. Coniglio, C. C. Agosta, A. Gurevich, and R. Prozorov, “Anisotropic upper critical field and possible Fulde-Ferrell-Larkin-Ovchinnikov state in the stoichiometric pnictide superconductor LiFeAs ,” *Phys. Rev. B* **83**, 060502(R) (2011).
- [30] A. A. Gurevich, “Iron-based superconductors at high magnetic fields,” *Rep. Prog. Phys.* **74**, 124501 (2011).
- [31] B. Maiorov, P. Mele, S. A. Baily, M. Weigand, S. Z. Lin, F. F. Balakirev, K. Matsumoto, H. Nagayoshi, S. Fujita, Y. Yoshida, Y. Ichino, T. Kiss, A. Ichinose, M. Mukaida, and L. Civale, “Inversion of the upper critical field anisotropy in FeTeS films,” *Superconductor Science and Technology* **27**, 0–6 (2014).
- [32] G. Fuchs, S. L. Drechsler, N. Kozlova, M. Bartkowiak, J. E. Hamann-Borrero, G. Behr, K. Nenkov, H. H. Klauss, H. Maeter, A. Amato, H. Luetkens, A. Kwadrin, R. Khasanov, J. Freudenberger, A. Köhler, M. Knupfer, E. Arushanov, H. Rosner, B. Büchner, and L. Schultz, “Orbital and spin effects for the upper critical field in As-deficient disordered Fe pnictide superconductors,” *New Journal of Physics* **11**, 0–26 (2009).
- [33] Rustem Khasanov, William R. Meier, Yun Wu, Daixiang Mou, Sergey L. Bud’ko, Ilya Eremin, Hubertus Luetkens, Adam Kaminski, Paul C. Canfield, and Alex Amato, “In-plane magnetic penetration depth of superconducting $\text{CaKFe}_4\text{As}_4$,” *Phys. Rev. B* **97**, 140503(R) (2018).
- [34] Mika Kano, Yoshimitsu Kohama, David Graf, Fedor Balakirev, Athena S. Sefat, Michael A. McGuire, Brian C. Sales, David Mandrus, and Stanley W. Tozer, “Anisotropy of the Upper Critical Field in a Co-Doped BaFe_2As_2 Single Crystal,” *Journal of the Physical Society of Japan* **78**, 084719 (2009).
- [35] M. Bristow et al., “Upper critical fields across the nematic end point in $\text{FeSe}_{1-x}\text{S}_x$,” in preparation (2019).
- [36] Hiroshi Kontani and Seiichiro Onari, “Orbital-Fluctuation-Mediated Superconductivity in Iron Pnictides: Analysis of the Five-Orbital Hubbard-Holstein Model,” *Phys. Rev. Lett.* **104**, 157001 (2010).
- [37] D. V. Efremov, M. M. Korshunov, O. V. Dolgov, A. A. Golubov, and P. J. Hirschfeld, “Disorder-induced transition between s_{\pm} and s_{++} states in two-band superconductors,” *Phys. Rev. B* **84**, 180512(R) (2011).
- [38] A. A. Golubov, J. Kortus, O. V. Dolgov, O. Jepsen, Y. Kong, O. K. Andersen, B. J. Gibson, K. Ahn, and R. K. Kremer, “Specific heat of MgB_2 in a one- and a two-band model from first-principles calculations,” *Journal of Physics Condensed Matter* **14**, 1353–1360 (2002).
- [39] Leonard W. Gruenberg and Leon Gunther, “Fulde-Ferrell Effect in Type-II Superconductors,” *Phys. Rev. Lett.* **16**, 996–998 (1966).
- [40] Tetsuro Saito, Youichi Yamakawa, Seiichiro Onari, and Hiroshi Kontani, “Revisiting orbital-fluctuation-mediated superconductivity in LiFeAs : Nontrivial spin-orbit interaction effects on the band structure and superconducting gap function,” *Phys. Rev.*

B **92**, 134522 (2015).

APPENDIX

In this section we present additional data to support the findings presented in the main paper.

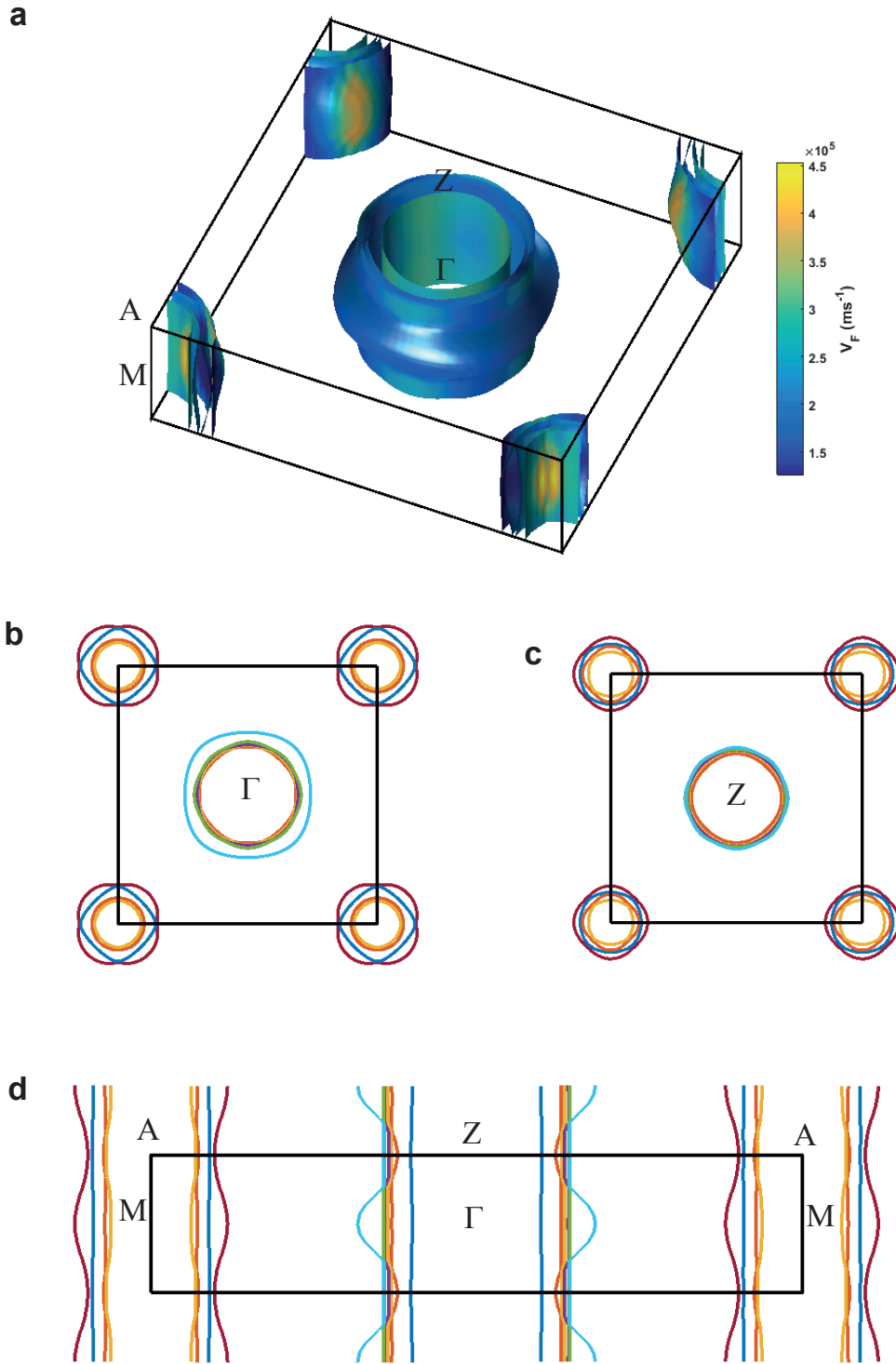


FIG. 4. **Fermi surface of $\text{CaKFe}_4\text{As}_4$.** a) Fermi surface with velocity colour. Slices at the b) Γ and b) Z point indicating the size of the different sheets. Solid lines indicate the Brillouin zone. c) Fermi surface slice along the $[110]$ diagonal of the Brillouin zone indicated by the solid lines. The calculations were performed using Wien2k and GGA approximation and the experimental lattice parameters described by the $P4/mmm$ symmetry group were $a=b=3.86590 \text{ \AA}$, $c=12.88400 \text{ \AA}$ [5]. The calculated value of anisotropy, $\Gamma=\lambda_c/\lambda_{ab}=313.68/70=4.5$ using a similar approach used in Ref.21. These calculations are in agreement with previous results reported in Ref. 22.

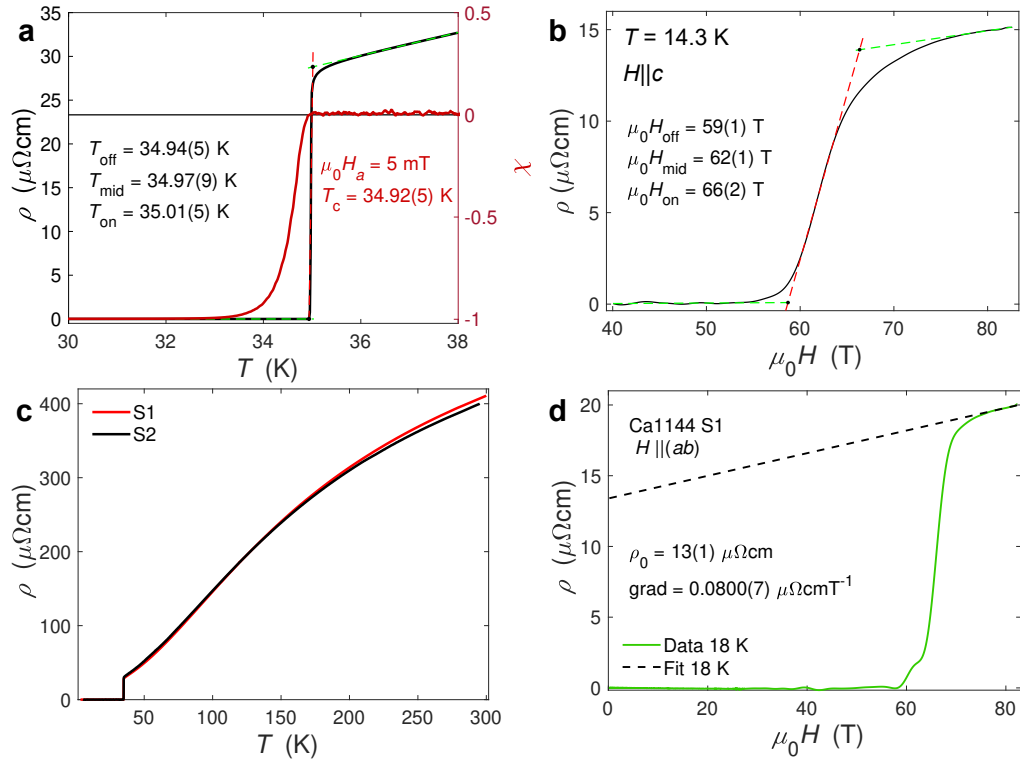


FIG. 5. Transport data of CaKFe₄As₄ as a function of temperature and magnetic field. (a) Estimating the critical temperature, T_c , from resistivity against temperature in zero magnetic field (left-axis) and from magnetic susceptibility in a small applied field of 5 mT (right-axis). The midpoint of the transition, T_{mid} , is identified as the peak in the derivative $d\rho/dT$. Linear fits are performed above and below the midpoint transition and the intercepts are defined as T_{off} and T_{on} , as labelled in the figure. T_c from susceptibility is defined as the point at which diamagnetism occurs and deviates from the high-temperature background and it is closest to the offset temperature in transport. The critical temperatures used to build the phase diagrams in magnetic field were extracted using T_{off} from the transport data. (b) The estimation of the upper critical field, H_{off} , from resistivity in pulsed magnetic field data measured at constant temperature using the same method as in (a). (c) Resistivity against temperature for different samples of CaKFe₄As₄ between 300 K and 2 K. The superconducting transition is very sharp, with $T_{c,0} = 35.0$ K and width $\Delta T_c = 0.15$ K, values typical for all measured single crystals indicating their high quality. (d) Resistivity data as a function of magnetic field for the sample S1 when $H||(ab)$ at 18 K. The dashed black line shows the linear extrapolation used to obtain the zero-field resistivity at 18 K and the intercept, $\rho_{H \rightarrow 0}(T)$, and gradient are shown. Using this method, the extracted values of zero-field resistivity measured at constant temperatures are shown in the main paper in Fig. 1(f).

A. Experimental details.

Several high quality single crystals were used in this study with large residual resistivity ratios $RRR = \rho(300\text{K})/\rho(36\text{K}) \sim 14.5$, small ρ_0 values of $\sim 9.2 \mu\Omega\text{cm}$ and sharp superconducting transitions with $\Delta T_c \sim 0.1 \text{ K}$, as shown in Figs. 5(c) and Fig.1(f). Temperature sweeps were performed at constant magnetic field for different orientations, $H||c$ and $H||(ab)$ to build the high-temperature part of the $H_{c2}(T)$ phase diagram. Magnetic fields up to 90 T were produced by using current pulses through two different solenoid coils. An example of the magnetic field produced as a function of time is shown in Fig. 6.

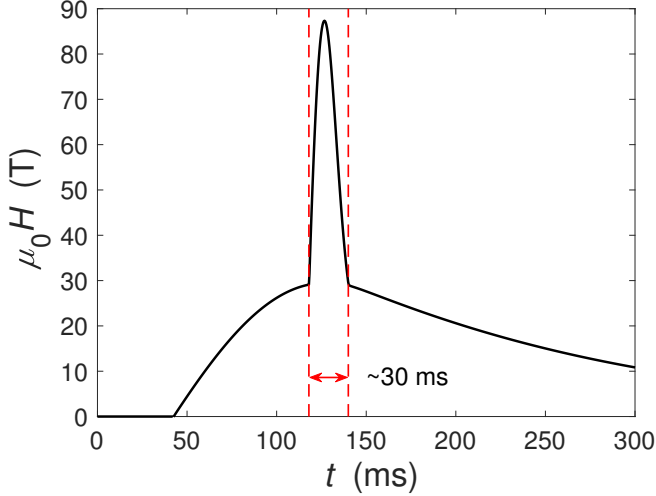


FIG. 6. **Generation of the high-magnetic field pulse.** Applied magnetic field as a function of time from the 90 T magnet in Toulouse. The peak of this pulse was $\sim 88 \text{ T}$ and is generated by overlaying pulsed current through two different coils. The pulse on the inner coil which generates the extremely high fields lasts $\sim 30 \text{ ms}$.

B. Determining superconducting coherence lengths.

The superconducting coherence lengths can be found in both field orientations near T_c using the Ginzburg-Landau (GL) approach from the equations:

$$\xi_{ab}^{\text{GL}} = \sqrt{\frac{\Phi_0}{2\pi\mu_0 \left| \frac{dH_{c2}^c}{dT} \right|_{T_c} T_c}}, \quad \xi_c^{\text{GL}} = \frac{\Phi_0}{2\pi\mu_0 \left| \frac{dH_{c2}^{ab}}{dT} \right|_{T_c} T_c \xi_{ab}^{\text{GL}}}, \quad (1)$$

where Φ_0 is the magnetic flux quanta, $\mu_0 |dH_{c2}^c/dT|_{T_c}$ is the slope near T_c when $H||c$, $\mu_0 |dH_{c2}^{ab}/dT|_{T_c}$ is the slope near T_c when $H||(ab)$ and ξ_{ab}^{GL} and ξ_c^{GL} are the respective GL coherence lengths.

At the lowest temperature, the coherence lengths are extracted using $\mu_0 H_{c2}(T \rightarrow 0)$ and the following equations:

$$\xi_{ab} = \sqrt{\frac{\Phi_0}{2\pi\mu_0 H_{c2}^c(T \rightarrow 0)}}, \quad \xi_c = \frac{\Phi_0}{2\pi\mu_0 H_{c2}^{ab}(T \rightarrow 0) \xi_{ab}}, \quad (2)$$

where ξ_{ab} and ξ_c are the coherence lengths in the (ab) -plane and along the c -axis, and $\mu_0 H_{c2}^c(T \rightarrow 0)$ and $\mu_0 H_{c2}^{ab}(T \rightarrow 0)$

are the critical fields at the lowest temperature when $H||c$ and $H||(ab)$ respectively. Using equations 2 at different temperatures, one can estimate $\xi_i \rightarrow \xi_i(T)$ and $H_{c2} \rightarrow H_{c2}(T)$, and the anisotropy ratio, Γ , as shown in Fig.2(b) in the main text.

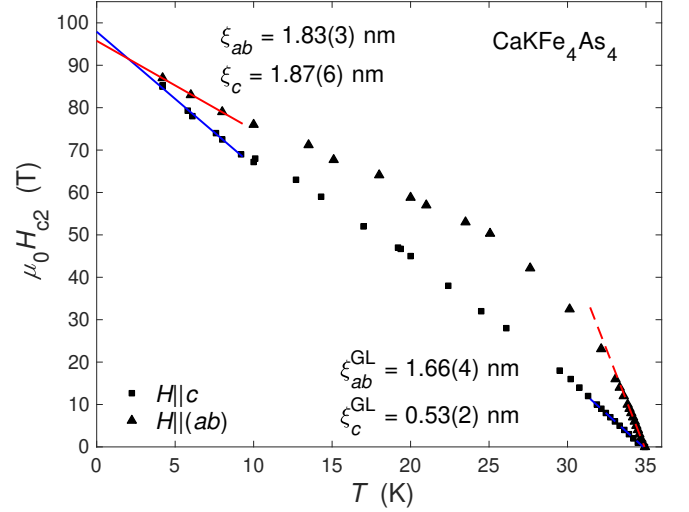


FIG. 7. **Coherence length extraction.** Upper critical fields in $\text{CaKFe}_4\text{As}_4$ as a function of temperature. The dashed blue and red lines are linear fits near T_c when $H||c$ and $H||(ab)$ respectively. The gradients of these fits (shown in the figure) were used to calculate the coherence lengths using the Ginzburg-Landau theory (equation 1). The solid blue and red lines are linear fits to the low temperature region when $H||c$ and $H||(ab)$ respectively. The zero-temperature extrapolation of $H_{c2}(T \rightarrow 0)$ for the two orientations were used to find the zero-temperature coherence lengths, as shown in the figure.

C. Depairing current density

Using the coherence length, one can also determine the critical depairing current density of a superconductor, J_d . As a function of temperature and magnetic field, this is expressed as [24]:

$$J_d(T, H) = \frac{2}{3\mu_0\lambda^2(T)} \sqrt{\frac{\mu_0(H_{c2}^2(T) - H^2)^{1/2}\Phi_0}{6\pi}}, \quad (3)$$

where λ is the superconducting penetration depth and Φ_0 is the magnetic flux quantum. At zero temperature and in no magnetic field, this gives

$$J_d(0, 0) = \frac{2}{3\mu_0\lambda^2(0)} \sqrt{\frac{\mu_0 H_{c2}(0)\Phi_0}{6\pi}}. \quad (4)$$

Substituting $\mu_0 H_{c2} = \Phi_0/2\pi\xi^2$ this equation can be rearranged to give

$$J_d(0, 0) = \frac{\Phi_0}{3\sqrt{3}\pi\mu_0} \frac{1}{\lambda^2(0)\xi(0)}. \quad (5)$$

Previous magnetisation reported $\mu_0 H_{c1} = 22(1) \text{ mT}$ [14] when $H||c$ at low temperature which, combined with H_{c2} values reported here, give $\kappa \sim 99(2)$ and $\lambda = 183(6) \text{ nm}$. Using

$\xi = 1.86$ nm, we find that the depairing current density is $J_d \sim 1.62 \times 10^8$ A/cm², which is among the largest of any known iron-based superconductor.

D. The upper critical fields using a two-band model.

To describe the entire temperature dependence of $H_{c2}(T)$ for CaKFe₄As₄, including the upturn below ~ 10 K for both orientations, we use a two-band model in the clean limit. This model includes paramagnetic effects and allows the emergence of a FFLO state, as detailed in Ref. 1. The values of the upper critical field for different temperatures are found from estimating the following expressions:

$$a_1[\ln t + U_1] + a_2[\ln t + U_2] + [\ln t + U_1][\ln t + U_2] = 0, \quad (6)$$

where $a_1 = (\lambda_0 + \lambda_-)/2w$, $a_2 = (\lambda_0 - \lambda_-)/2w$, $\lambda_{\pm} = \lambda_{11} \pm \lambda_{22}$, $w = \lambda_{11}\lambda_{22} - \lambda_{12}\lambda_{21}$ and $\lambda_0 = (\lambda_{\pm}^2 + 4\lambda_{12}\lambda_{21})^{1/2}$. Here λ_{ij} represents a coupling constant between bands i and j , and as the cross-terms λ_{12} and λ_{21} only appear together we set $\lambda_{21} = \lambda_{12}$ for simplicity. The values of the coupling constants allows us to establish the dominant pairing. For s^{++} pairing the parameter $w > 0$ ($w \sim 0.248$ for the case presented in Fig. 3(c) and Fig. 9(c)) whereas for s^{\pm} pairing $w < 0$ (Fig. 3(a) and (b), and Figs. 9(a) and 9(b)).

U_1 and U_2 are defined as

$$U_1 = 2e^{q^2} \text{Re} \sum_{n=0}^{\infty} \int_q^{\infty} du e^{-u^2} \left(\frac{u}{n+1/2} - \frac{t}{\sqrt{b}} \tan^{-1} \left[\frac{u\sqrt{b}}{t(n+1/2) + i\alpha b} \right] \right) \quad (7)$$

$$U_2 = 2e^{q^2 s} \text{Re} \sum_{n=0}^{\infty} \int_{q\sqrt{s}}^{\infty} du e^{-u^2} \left(\frac{u}{n+1/2} - \frac{t}{\sqrt{b\eta}} \tan^{-1} \left[\frac{u\sqrt{b\eta}}{t(n+1/2) + i\alpha b} \right] \right) \quad (8)$$

The variables used for this two-band model, b , α , q , η and s , are defined as

$$b = \frac{\hbar^2 v_1^2 H_{c2}}{8\pi\phi_0 k_B T_c^2}, \quad \alpha = \frac{4\mu\phi_0 k_B T_c}{\hbar^2 v_1^2}, \quad q^2 = \frac{Q^2 \phi_0 \epsilon_1}{2\pi H_{c2}}, \quad \eta = \frac{v_2^2}{v_1^2}, \quad s = \frac{\epsilon_2}{\epsilon_1}. \quad (9)$$

v_i is the in-plane Fermi velocity of band i , ϵ_i is the mass anisotropy ratio, $\epsilon_i = m_i^{\perp}/m_i^{\parallel}$ is related to the ratio between the gradients near T_c in different field orientations, s is band

mass anisotropy between the two bands and $\gamma = \epsilon^{-1/2}$. Various simulations of upper critical fields using this two-band model are shown in Fig. 8. The slope of H_{c2} near T_c of CaKFe₄As₄, is -3.3 for $H||c$ and -10.8 for $H||(ab)$, giving an $\epsilon \sim 1/10$. Q is the magnitude of the FFLO modulation and it is found for a given temperature when H_{c2} is maximal ($dH_{c2}/dQ = 0$). The simulations of H_{c2} for $H||(ab)$ assumed that the bands have the same anisotropy parameter $\epsilon_1 = \epsilon_2 = \epsilon$. Other parameters are estimated based on the fitted values using a single-band model and the velocities are minimised locally to find an optimum solution. This approach was used for the two different s^{\pm} and s^{++} pairing, which are described in the main body.

A rescaling of the upper critical field has been performed previously mapping $H_{c2}^c \rightarrow H_{c2}^{ab}$ using $q_{ab} \rightarrow q_c \epsilon^{-3/4}$, $\alpha_{ab} \rightarrow \alpha_c \epsilon^{-1/2}$, $b_{ab}^{1/2} \rightarrow b_c^{1/2} \epsilon^{1/4}$ in U_1 , $(\eta_{ab} b_{ab})^{1/2} \rightarrow (\eta_c b_c^{1/2}) \epsilon^{1/4}$ in U_2 . The values of the α parameters change as $\alpha_{ab,1} \rightarrow \alpha_c \epsilon^{-1/2}$, and $\alpha_{ab,2} \rightarrow \alpha/(\eta \epsilon^{1/2})$. However, this rescaling has not been used in this study, as the ratio between the Fermi velocities η is a variable parameter that can be changed between the two field orientations.

Previous studies on CaKFe₄As₄ have described the onset upper critical field data up to 60 T using the parameters $\lambda_{11} = \lambda_{22} = 0$, $\lambda_{12}\lambda_{21} = 0.25$, $\eta = 0.2$, $\alpha = 0.5$ and $\epsilon = 1/6$ and the above re-scaling [7]. Using these parameters we find that the onset upper critical field data (open blue and red symbols) clearly fail to describe the full temperature dependence of the upper critical field of CaKFe₄As₄, as shown in Fig. 9(a) and (b) (blue and red curves). As discussed in the main body of text, we can reasonably describe the upper critical field of CaKFe₄As₄ using a two-band model with band parameters for the s^{\pm} and s^{++} pairing (see Table I), as shown in Fig. 9(c) and 9(e), respectively. We note here that an FFLO state can be stabilized at low temperatures for $H||(ab)$ (Fig. 9(c) and (e), right axis).

To further test the obtained parameters, we have modelled both the offset and onset critical fields for both field orientations assuming the s^{\pm} and s^{++} pairing. The parameters for the two cases are listed in Table I and the simulations of the upper critical field are shown in Fig. 9. We find that the parameters describing the offset and onset upper critical fields are similar, with small differences found for the α values, which are slightly larger as the curvature for H_{on} is greater as compared with the H_{off} case. The velocities for H_{on} are also slightly smaller due to the larger slopes near T_c , which scales as $|dH_{c2}/dT|_{T_c} \propto 1/v^2$. Using the values for H_{off} and H_{on} , we expected a $\sim 20\%$ difference in velocities when $H||c$, and a $\sim 10\%$ difference when $H||(ab)$, as shown in Table I. However, independent of the definition of the upper critical field, the stabilization of an FFLO state in CaKFe₄As₄ for $H||(ab)$ is realized in both cases.

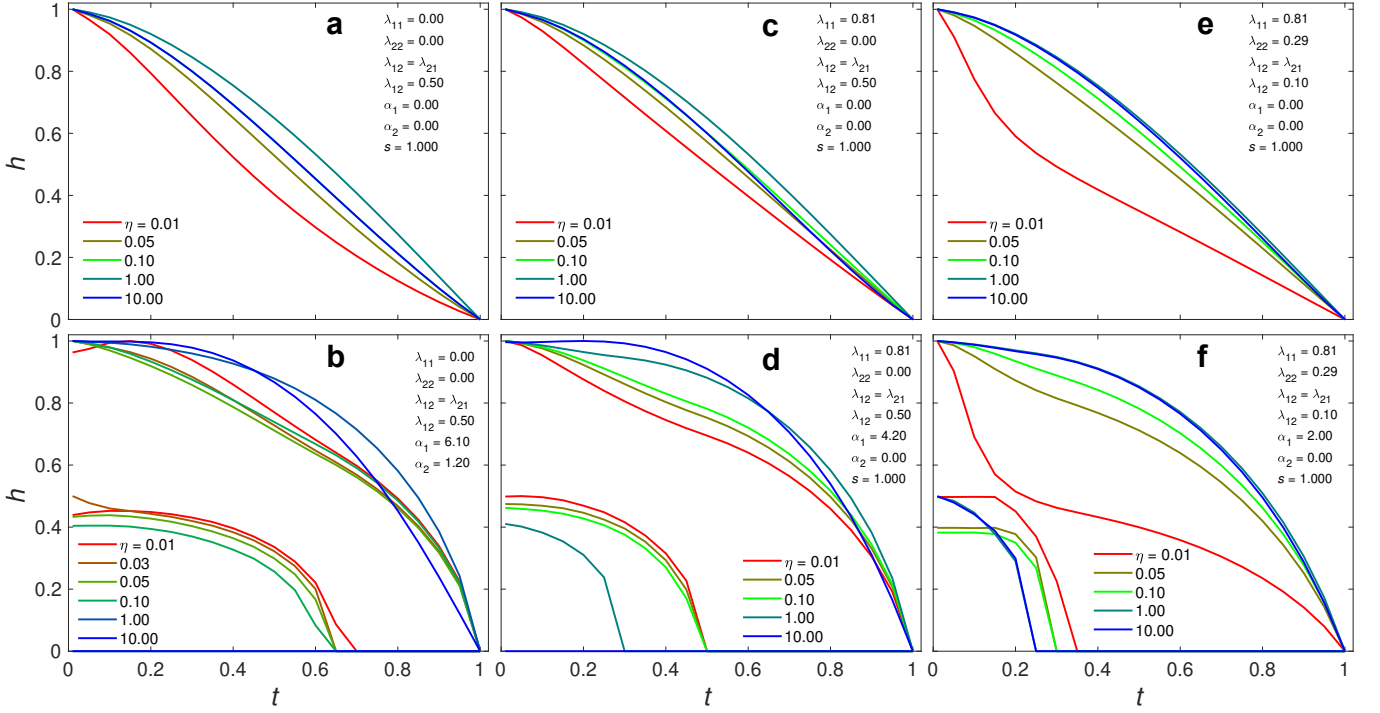


FIG. 8. **Two-band upper critical field simulations for different band coupling parameters and values of η .** Simulations of the reduced upper critical field h using the two-band model based on equations 6-9. The parameters listed in each panel correspond to s^\pm pairing in (a) and (b) with $\lambda_{11} = \lambda_{22} = 0$, $\lambda_{12} = \lambda_{21} = 0.5$, s^\pm pairing in (c) and (d) with $\lambda_{11} = \lambda_{22} = 0.81$, $\lambda_{12} = \lambda_{21} = 0.5$, and s^{++} pairing in (e) and (f) with $\lambda_{11} = 0.81$, $\lambda_{22} = 0.29$ and $\lambda_{12} = \lambda_{21} = 0.1$, $\alpha_1 = 0.95$ for $H||c$. For panels (b), (d) and (f) the lower curves (left corners) represent the magnitude of the FFLO modulation, $Q/(2Q(0))$.

TABLE I. The different parameters used for the simulations of the upper critical field (defined either using an offset or onset magnetic field) using a two-band model and considering different pairing symmetries and magnetic field orientations in CaKFe₄As₄.

	$\mu_0 H_{\text{off}}$				$\mu_0 H_{\text{on}}$			
	s^\pm		s^{++}		s^\pm		s^{++}	
	$H c$	$H (ab)$	$H c$	$H (ab)$	$H c$	$H (ab)$	$H c$	$H (ab)$
λ_{11}	0	0	0.81	0.81	0	0	0.81	0.81
λ_{22}	0	0	0.29	0.29	0	0	0.29	0.29
λ_{12}	0.5	0.5	0.1	0.1	0.5	0.5	0.1	0.1
α_1	0.95	3.1	0.5	3.2	1.5	4.2	1.0	3.5
α_2	0	0.7	0	0	0	0	0	0
v_1 (meVÅ)	510(20)	253(20)	380(20)	195(20)	400(20)	215(20)	312(20)	181(20)
v_2 (meVÅ)	40(4)	51(5)	54(4)	41(4)	36(3)	43(4)	44(4)	38(4)
η	~ 0.006	~ 0.04	~ 0.02	~ 0.04	~ 0.008	~ 0.04	~ 0.02	~ 0.045

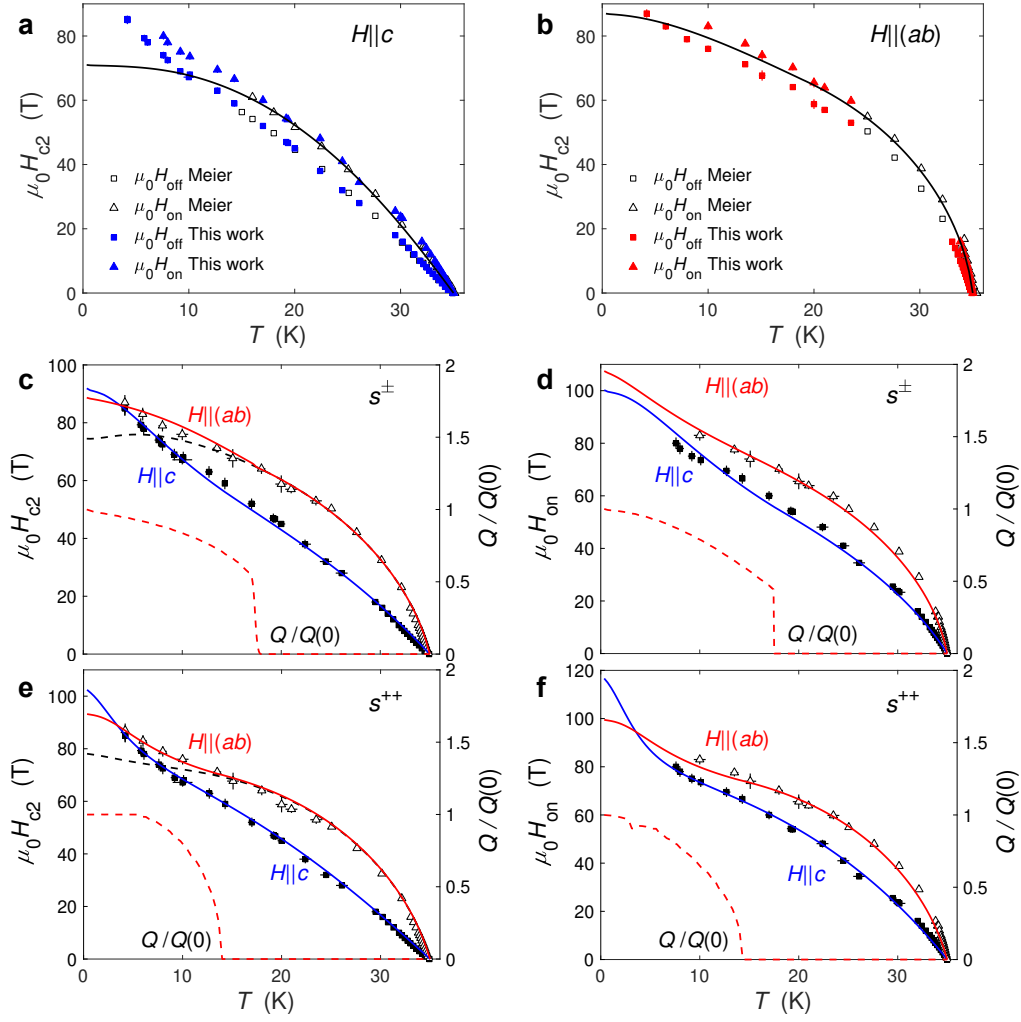


FIG. 9. **Two-band upper critical field models for $\text{CaKFe}_4\text{As}_4$ using different band coupling parameters.** (a) and (b) $\lambda_{11} = \lambda_{22} = 0$, $\lambda_{12}\lambda_{21} = 0.25$, $\eta = 0.2$, $\alpha = 0.5$ and $\epsilon = 1/6$ used previously to describe the onset upper critical field of $\text{CaKFe}_4\text{As}_4$ up to 60 T [7] when $H||c$ and $H||(ab)$ respectively. (c) s^\pm pairing with $\lambda_{11} = \lambda_{22} = 0$, $\lambda_{12} = \lambda_{21} = 0.5$. Here $\alpha_1 = 0.95$, $\alpha_2 = 0$ and $\eta \sim 0.006$ for $H||c$, and $\alpha_1 = 3.1$, $\alpha_2 = 0.7$ and $\eta \sim 0.04$ for $H||(ab)$. (d) s^\pm pairing for the onset critical field using the same parameters as in (c), but with $\eta \sim 0.008$ and $\alpha_1 = 1.5$ when $H||c$, and $\alpha_1 = 4.2$ when $H||(ab)$. (e) s^{++} pairing with $\lambda_{11} = 0.81$, $\lambda_{22} = 0.29$ and $\lambda_{12} = \lambda_{21} = 0.1$. Here $\alpha_1 = 0.95$, $\alpha_2 = 0$ and $\eta \sim 0.02$ for $H||c$, and $\alpha_1 = 3.1$, $\alpha_2 = 0.0$ and $\eta \sim 0.04$ for $H||(ab)$. (f) s^{++} pairing for the onset critical field using the same parameters as in (e), but with $\alpha_1 = 1.0$ when $H||c$, and $\alpha_1 = 3.5$ when $H||(ab)$. In (c)-(f) blue lines show the two-band model (with no FFLO state present) when $H||c$, dashed black lines show the two-band model with no FFLO state when $H||(ab)$, and the red lines show the two-band model with an FFLO state when $H||(ab)$. The temperature dependence of the FFLO Q vector is shown by the dashed red lines (the right-axis in (c)-(f)) for $H||(ab)$, and it is scaled to the zero-temperature value $Q(0)$. We note that the FFLO state emerges when $H||(ab)$ regardless of the pairing limit or which critical field criteria is chosen. This reinforces the robustness of this result.